24th EUROPEAN ROTORCRAFT FORUM

Reference AE14

A Detailed Comparison of DLR and ONERA 3D Euler Methods for Rotors in High Speed Forward Flight

Klausdieter Pahlke, DLR, Institute of Design Aerodynamics

Jean-Christophe Boniface, ONERA, Computational Fluid Dynamics and Aeroacoustics Department

This paper compares the ONERA deforming grid and the DLR chimera Euler method for isolated rotors in high speed forward flight.The following investigations were carried out: Using the DLR chimera method the effect of the far field distance, of introducing an artificial hub boundary and of changing the position of the blade root were investigated. The sensitivity of the method to the dihedral of the blade was shown by running one computation without dihedral. The ONERA and DLR methods are compared in terms of pressure coefficients, z-force coefficients and vorticity plots. The overall agreement of the methods with each other and with the experimental data for the ONERA PF1 rotor in high speed forward flight is very good.

List of symbols:

c	local chord
c_∞	speed of sound of the free stream
c_p	pressure coefficient $\dfrac{p - p_\infty}{\frac{1}{2}\rho_\infty(\omega r + \omega R\mu\sin\psi)^2}$
F_z	force in z-direction
M	Mach number
$M_{\omega R}$	$\omega R / c_\infty$
p	pressure
r	radial position
R	rotor radius
t	time
u, v, w	Cartesian velocity components
V_∞	free stream velocity
x, y, z	Cartesian coordinates
z-axis	axis of rotation, positive up
β	flapping angle, positive up
θ	pitching angle
μ	advance ratio $V_\infty/(\omega R)$
ρ	density
ψ	azimuth
ω	angular velocity ($\omega = d\psi/dt$)

Lower index:

∞	free stream value

1. Introduction

Within the ONERA/DLR cooperation on Rotorcraft CFD Code Development a detailed comparison of the existing 3D Euler methods for isolated rotors in forward flight with pure capture of the wake was carried out.

A preliminary comparison of the ONERA and DLR Euler methods was done in [1] based on two test cases: the 3-bladed PF1 rotor and the 4-bladed 7AD rotor in high speed forward flight. Although an acceptable overall agreement was achieved the quantitative comparison of the prediction methods was not favourable. With respect to the 7AD test case it turned out that the DLR computation was run with a flapping motion which considers the Fourier harmonics up to second order while the ONERA computation used only the 0-th and 1-st order Fourier harmonics. After repeating the computation with the same flapping motion the quantitative agreement of the two predictions was acceptable. This raises the question why the quantitative agreement of the two prediction methods is less good for the PF1 rotor, which is referred to as a classical test case for validation of CFD methods in the literature.

So it was decided to concentrate the comparison of the two methods on the PF1 rotor. This com-

parison was carried out when the first author spent 3 months as an exchange scientist at the ONERA Research Center in Châtillon.

The ONERA Euler method for rotors in high speed forward flight with pure capture of the wake which uses a deforming grid strategy and the corresponding DLR method which is based on a chimera approach are described in chapter 2. The experimental setup is recalled in chapter 3 and the grids for the computations are described in some detail in chapter 4. Generating classical non-overlapping block-structured grids around helicopter rotors it is very difficult to close the grid at the axis of rotation. In order to avoid highly stretched and sheared grid cells a first grid plane in radial direction is defined as a part of a cylinder with a finite radius. Since this cylinder is placed at a position where in reality the rotor hub would be (typically with a much smaller radius) the term "artificial hub boundary" is used throughout this paper for the first grid boundary next to the axis of rotation (see figure 1). For chimera grids it is not necessary but possible to introduce such an "artificial hub boundary".

The following investigations were carried out. Using the DLR chimera method the effect of the far field distance, the effect of introducing an artificial hub boundary and the effect of the position of the blade root were investigated (see chapter 4.1). Then the sensitivity of the method to the blade dihedral was investigated (see chapter 4.2). It turned out that the dihedral of the PF1 blade was not correctly modelled in the grids which were used in [1]. Chapter 4.3 compares the ONERA and the DLR prediction using the correct blade dihedral with each other and with the experimental data. For all computations of chapter 4.3 the chimera method uses a CH-type child grid which was extracted out of the ONERA multiblock grid. This guarantees that exactly the same geometry and the same point distribution near the blade is used in both methods.

2. Description of the Methods

Both methods are described in detail in [1]. Thus only the main features are repeated in the following.

2.1 DLR: Numerical Algorithm and Grid Generation

The unsteady Euler equations in integral conservation law form have been transformed into a moving blade-fixed coordinate system. The velocities are referred to the moving coordinate system but they are formulated without any metric dependent terms (i.e. in terms of absolute velocity or velocity of the fluid relative to an inertial frame of reference). Due to this formulation a source term is introduced which contains the trigonometric functions describing the rotational motion.

The discretization of space and time is separated following the method of lines (Jameson et. al. [2]) using a cell-centred finite-volume formulation for the spatial discretization. The scheme is of second order spatial accuracy on smooth grids. In order to avoid spurious oscillations, a blend of first and third order dissipative terms is introduced. An explicit five-stage second-order Runge-Kutta time stepping scheme is used with an evaluation of the dissipative fluxes at the first two stages [2]. The technique of implicit residual averaging has been adapted to time-accurate computations [3].

A zero flux condition is used at the surface of solid bodies. The far field boundary is treated following the concept of characteristic variables for non-reflecting boundary conditions [4]. Auxiliary cells are used to store the neighbour flow values in order to match the solution across inner cuts. In order to have second-order spatial accuracy at inner cuts two layers of auxiliary cells are used.

The code allows to use any kind of block stuctured grids (e.g. OO-, OH-, CH-, HH-topologies, etc.) with an arbitrary number of blocks.

In order to allow for the relative motion of the blades of a rotor an overlapping grid algorithm (chimera algorithm) is used (see [1],[5] and [6]). Figure 2 shows a set of three child or nearfield grids embedded into a cylindrical father or background grid for the three-bladed ONERA model rotor. In this implementation only flow values are exchanged at the chimera boundaries. In order to provide the flow values at the grid interfaces it is necessary to use interpolation formulae. A linear interpolation based on tetrahedrons (3D) was chosen (see [7]).

The DLR child grids around the rotor blades use an OH-topology with the O in the wrap around direction and the H in the radial direction. The grids are 3D elliptically smoothed [8] which increases the accuracy and makes the search algorithm of the chimera scheme more efficient.

2.2 ONERA: Numerical Algorithm and Grid Generation

In the ONERA method, the unsteady Euler equations are formulated in integral conservation law form in an inertial frame (the one linked to the helicopter fuselage) using the absolute velocity referred to this frame. Thus the conservative variables are formulated without any metric dependent terms and there are no source terms. The numerical scheme is based on a multidimensional version of the Lax-Wendroff scheme, in predictor-corrector form. This predictor-corrector version is of S_{β}^{α} type

with one predictor in each space direction, and was developed by Lerat and Sidès for two-dimensional unsteady transonic Euler flow simulations [9], [10]. An explicit and an implicit stage are solved at each time step. The explicit stage gives the overall second-order accuracy of the approximation (on a cartesian grid), with reduced dispersion errors and good dissipation properties. However, the internal dissipation of the scheme needs to be strenghtened by a second-order quasi-TVD correction. The implicit stage reduces to a Scalar Approximate Factorisation (ADI factorisation with spectral radius technique). This implicit treatment brings a very important saving in computational effort because the linear systems to be solved are simply tridiagonal and not block-tridiagonal.

An accurate treatment of the slip condition at the surface of the blades is achieved by a conservative discretization of the unsteady mass conservation and the normal momentum equations in the finite-volume approach. This conservative treatment expresses the pressure at the blade surface without requiring any interpolation. Free stream conditions based on characteristic theory but in terms of primitive variables are applied at the outer boundaries in the radial and axial directions and also on the artificial hub boundary.

The ONERA method uses a multi-block structured grid which encloses the whole multi-bladed rotor, where each block is generated around a single blade with a C-H cylindrical topology with angle $2\pi/N$, N being the number of blades. An exact connection between the blocks is ensured (see figure 1 for the 3-bladed ONERA model rotor). The blade motions are taken into account within a moving grid approach while keeping fixed the outer boundaries. Details can be found in [11]. The features of this moving grid approach allow for the transfer of information throughout the whole computational domain without any interpolation technique involved.

3. Description of the Experimental Setup

The test case chosen is the flow around the 3-bladed ONERA model rotor in lifting forward flight with PF1 tips. This rotor has straight blades up to 0.8 R with a chord of c_{ref}=123 mm. At 0.8 R removable tips are fastened to the blades (see [12]). Different sets of blade tips have been tested: straight tips, swept back tips without dihedral and swept back tips with dihedral. Here a parabolic swept back tip (PF1-tip) with dihedral is investigated. The blades have an aspect ratio R/c of 7. The blade airfoils are SA131XX airfoils. This rotor was tested in the S2 Chalais-ONERA wind tunnel (see ([13])). One blade was instrumented at three spanwise stations (0.85R, 0.90R and 0.95R). The rotational tip Mach Number is $M_{\omega R} = 0.613$ with an advance ratio of $\mu = 0.4$ and a free stream Mach number of $M_\infty = 0.2452$. The rotor shaft angle is equal to $-12.4°$. The flapping and pitching motions of the blades are given by:

$$\theta = 14.16° + 0.43°\cos\psi - 5.14°\sin\psi$$

$$\beta = 1.25° - 5.12°\cos\psi + 0.32°\sin\psi \quad .$$

These laws were provided by the R85/ METAR code [14].

4. Numerical Results

4.1 Gridding Parameters

The DLR and the ONERA method use two different grid strategies.

For the ONERA moving grid approach (see chapter 2.2) the artificial hub boundary has a radius of 0.18 R (see figure 1). The ONERA grid consists of three blocks where each block has 116 cells in wraparound direction, 16 cells in normal direction and 26 cells in radial direction (total 48 256 cells per block).

The DLR method uses the so called chimera method as it has been described in chapter 2.1. Therefore a relatively simple background grid can be used. Figure 3 shows two views of the background grid. The Z-axis is the axis of rotation and the X-axis points in the direction of the free stream. The background grid in figure 3 has a far field distance from the center of the rotor disk of about 3R in all directions. The far field distance from the blade tip in radial direction is more than 2R. This grid will be referred to as "R_{FF}=3R". It has 90 cells in azimuthal direction, 40 cells in axial direction and 28 cells in radial direction with a total number of grid cells of 100 800. A second background grid was generated by skipping the outer grid lines of the "R_{FF}=3R"-grid such that a grid with a far field distance to the blade surface of at least 1R is achieved. This grid is referred to as "red. FF dist." (reduced Far Field distance). A third background grid was generated by skipping the first inner sections of the "R_{FF}=3R"-grid, such that an artificial hub boundary with a radius of 0.3 R is achieved. This grid is presented in figure 4. This grid will be referred to as "r_{hub}/R=0.3". It should be noted, that the "red. FF dist."- and the "r_{hub}/R=0.3"-grid have exactly the same grid points in the common regions as the original grid. The blade geometry is contained in the child grids which are embedded into the background grids.

Figure 5 shows a cross section at 0.85 R of one blade of the grid of cell centers. In the left part of the figure the background grid is shown with the hole cells blanked out. The right part of figure 5 shows an OH-type child grid embedded into the background grid. The corresponding figure for a longitudinal section is given in figure 6. The grid density in the vicinity of the outer boundaries of the child grid is very similar in the background grid and the child grid. Hence a solution of similar accuracy can be expected in the hole computational domain. It should be noted that figures 5 and 6 show only the inner cells. The DLR OH-type child grids in this paper have 64 cells in the wraparound direction, 16 cells in the normal direction and 27 cells in radial direction (total 27 648 cells). The CH-type child grids extracted out of the ONERA grids are embedded in the same manner. They have 106 cells in streamwise direction, 14 cells in normal direction and 24 cells in radial direction (total 35 616 cells). The point distribution of the CH-grids has not been adapted to the chimera background grids.

The application of the chimera method is much easier with blades which have a finite thickness only between the blade root and the blade tip. The rotor head is not modelled (see figure 7, top). Using this simplification there is no need for an artificial hub boundary in the computation. The DLR computations in this paper use a position of the blade root of 0.276 R if no other value is explicitly stated. This means that the first section with a SA13112 Airfoil is at r/R=0.276 which is the blade root position of the model rotor blade. Figure 7 illustrates the different gridding of the two approaches close to the axis of rotation.

4.1.1 Effect of Far Field Distance

In order to check whether a sufficiently large far field distance was chosen, two computations were carried out. One computation using the "R_{FF}=3R"-grid as background grid and another using the "red. FF dist."-grid as background grid. The OH-type child grid of [1] was used for this comparison. Figure 8 shows the non-dimensionalized z-force-coefficient

$$c_z * M^2 = \frac{F_z}{0.5 \cdot \rho_\infty \cdot c_\infty^2 \cdot c \cdot dr}$$

at three sections for the two grid systems. It is obvious, that the reduced far field distance is sufficient since the numerical results are identical for the two far field distances used.

4.1.2 Effect of the Blade Root Position and of the Artificial Hub Boundary

In order to investigate the effect of the artificial hub boundary in the conventional grid it was decided to make a chimera computation with an artificial hub boundary at 0.3R. The chimera method requires some inner cells between the artificial hub boundary and the blade root. Therefore it was not possible to use the blade with the original blade root position for this computation. A second child grid was generated with a blade root at r_{root}/R=0.4. This was done by modifying the original OH-type child grid only in the vicinity of the blade root. So all grid points with r/R larger than r/R=0.4 have not been touched.

The resulting grid system differs from the R_{FF}=3R-grid system in two aspects:

- the introduction of the artificial hub boundary,
- the position of the blade root.

In order to isolate the effects two computations were carried out. The first computation uses the R_{FF}=3R-background grid with the r_{root}/R=0.4-child grid. The second computation uses the "r_{hub}/R=0.3"-background grid with the r_{root}/R=0.4 child grid.

Figure 9 compares the $c_z * M^2$-values for the two positions of the blade root and the same background grid (R_{FF}=3R) with the computation with an artificial hub boundary (background grid: r_{hub}/R=0.3, child grid: r_{root}/R=0.4). There is a considerable increase of the normal force coefficient for all five sections for $0<\psi<60^o$. Due to the artificial hub boundary there is an additional increase of the z-force coefficient in about the same region of the azimuth angle. These effects cannot be neglected even for r/R=0.95. For azimuthal angles larger than 60^o the effects are less pronounced. It should be noted that a weak interaction between the tip vortex and the following blade is predicted at about $\psi=75^o$.

Figures 10 - 12 present the corresponding pressure distributions. The effective angle of attack for the solutions with r_{root}/R=0.4 is increased for $0<\psi<60^o$ degrees.

In order to understand this behaviour the vorticity distribution in the flowfield was investigated. This was done in the following manner. First all velocities are non-dimensionalized by the velocity of the speed of sound of the free stream c_∞. All

coordinates are non-dimensionalized by the chord length c_{ref}. The velocity field for ψ_{Blade1}=60° (figure [13]) is used for the computation of the vorticity:

$$\Gamma = \left| rot \begin{bmatrix} u \\ v \\ w \end{bmatrix} \right| .$$

Figure 13 gives an overview of the vortex trajectories which can be detected in the solution for a computation with the "R_{FF}=3R"=background grid and the OH-type child grid with r_{hub}/R=0.276. This figure was generated by defining slices of the 3D solution which contain the axis of rotation and which are inclined to the x-axis by ψ = 15°, 30°, 45°, ..., 180°. The coordinates of the centers of the clearly distinctible vortex structures where picked from the different slices using the tecplot software and written into a file. After an age of about 120° the tip vortices are so strongly diffused that they cannot be traced further. In order to produce some pictures that can easily be interpretated it was decided to define sections perpendicular to the direction of the main flow which is in the case of a rotor in highspeed forward flight the x-direction. So 6 slices were defined normal to the x-axis at x=-3.0, 0.0, 1.5, 3.0, 4.5 and 6.0. The positions of these slices are indicated in figure 13. Only the most interesting slices will be presented in the following. Figure 14 compares the vorticity distributions for two different positions of the blade root, i.e. r_{root}/R=0.276 and r_{root}/R=0.4 at x=4.5 and x=6.0. It should be noted that this means a shift of the blade root position of almost one chord {(0.4-0.276)*R=0.868 c}. The blade root position of r_{root}/R=0.4 is indicated by a dash-dotted line in figure 13. For x=4.5 a much stronger root vortex of blade 1 (R1) is computed for the r_{root}/R=0.4 geometry (see figure 14). It is obvious that such a vortex will interact with the following blade by locally increasing the effective angle of attack. A similar situation is given at x=6.0 but with a much weaker vorticity structure. These observations explain the increase of the normal force coefficient for 0<ψ<60°. Figures 15 compares the vorticity distributions for a computation with an artificial hub boundary (r_{hub}/R=0.3) and without (r_{root}/R=0.4). At the artificial hub boundary the condition of undisturbed flow is applied. The effect of this boundary condition is obvious at the x=1.5 slice. All downwash velocities at the artificial hub boundary are replaced by the free stream values which do not contain any downwash component. Hence the effective angle of attack is higher behind the artificial hub boundary. This increased angle of attack increases the z-force-component as it is shown in figure 9. This effect cannot be neglected for 0<ψ<60°. Looking at figures 13 and 14 a weak interaction between blade 2 and the tip vortex of blade 1 can be seen (see also figure 9). The computed vortex passes below the blade and is highly diffused.

4.2 Effect of Dihedral

In order to show the sensitivity of the method to the dihedral of the PF1 blade two computations were carried out: one with dihedral and one without dihedral. The blade with dihedral uses the exact dihedral as the PF1-blade of the experiment.

Figure 16 presents the comparison of the computation with dihedral and without dihedral with the experiment. Close to the tip the computation without dihedral clearly overpredicts the z-force coefficients around ψ=180°. The computation with dihedral agrees well with the experimental data. The blade with dihedral produces higher z-force coefficients in the first and the fourth quadrant but lower z-force-coefficients in the second and the third quadrant.

4.3 Comparison of DLR and ONERA Results

The ONERA moving grid method and the DLR chimera method were applied to the same test case. A part of the ONERA grid was used as a child grid for the chimera computation. Hence exactly the same blade geometry and the same grid point distribution is used in the vicinity of the blade except for the blade root. In the ONERA computation a so called artificial hub boundary is used as it was described in chapters 2.2 and 4.1.2. Therefore the blade in the ONERA grid has no blade root in the interior of the grid and no root vortex is computed.

Figure 17 compares the z-force coefficient of the two computations which each other and with the experimental data. As expected there are some differences for 300°< ψ < 360° and for 0° < ψ < 60° for all 5 radial stations. For 60° < ψ < 300° the agreement of the two computations for r/R > 0.5 is excellent. The slightly larger differences at r/R=0.5 are due to the different treatment of the blade root in the two computations ("hub"/"no-hub", "no root vortex"/ "root vortex"). The agreement of the computations with the experimental data is very good. For 0° < ψ < 60° the DLR solution agrees slightly better with the experimental data. The increased z-force- coefficients of the ONERA solution are due to the artificial hub boundary in the moving mesh com-

putation. For $300^{o} < \psi < 360^{o}$ the ONERA solution is somewhat closer to the experimental data. This is again due to the artificial hub boundary, because the root vortex in the DLR computation is stronger than the root vortex in the real flow field. This is due to the fact that the real rotor blade has a blade root which consists of a part with an airfoil and a part without airfoil, the blade shaft, which is connected to the rotor head. This shaft without airfoil reduces the strength of the root vortex. In the computation the existance of the artificial hub boundary reduces the root vortex for the retreating blade which gives a slightly better agreement with the experimental data. The larger differences between both predictions and the experimental data at $\psi = 0^{o}$ are due to the mast which carries the rotor in the experiment and produces a strongly disturbed flow in the region of $345^{o} < \psi < 360^{o}$ and $0^{o} < \psi < 15^{o}$. It should be noted that no interaction between a vortex and a blade can be detected in figure 17. The resolution of the tip vortex is not sufficient in these grid systems. Figures 18 - 20 present the pressure distribution for three radial stations every 30^{o} azimuth. The agreement of the two computations with each other is excellent and the agreement with the available experimental data is very good. The differences can be explained like for the z-force-coefficients. The vorticity distributions for six slices as introduced in figure 13 are presented in figures 21 - 23 for the two computations. At x=-3.0 the vorticity distributions of the two computations show the same location of the centers of the vortices. The shape of the vortices is different. This is due to the fact that the grid close to the blade is finer in z-direction than the background grid of the chimera computation (see figures 6 and 7). So the vortex resolution for the moving grid computation at x=-3.0 is better. At this position the vortices are more diffused in the chimera computation. There are two major effects at x=0.0. The first effect is due to the artificial hub boundary in the moving mesh computation. This artificial boundary disturbs the vorticity distribution and reduces the downwash velocities close to the axis of rotation. The second effect is again the better resolution of the vortices due to the finer distribution of grid lines in the moving mesh computation. It should be noted that the vortices have the same location in both computations. A similar description can be given for x=1.5, but in addition it is obvious that a strong root vortex is visible in the chimera computation while there is no root vortex at all computed in the moving mesh computation. At x=3.0 the situation changes a little. There is again the effect of the artificial hub boundary which cancels a lot of vorticity in the vicinity of the axis of rotation. There is a weak vorticity structure at about y=-3 and z=-2 (T1) in the chimera computation while no such structure is computed in the moving mesh computation. The comparison with figure 13 shows that this weak structure is a trace of the tip vortex of blade number 1. The situation at x=4.5 is very similar to the situation at x=3. In the DLR computation some traces of the tip vortex of blade 1 (T1) can still be seen, while the ONERA computations does not show any traces of this vortex. The reason is the different point distribution in the two grid systems. The ONERA grid is finer close to the blade than the DLR background grid but far away from the blade the ONERA grid is highly nonregular and coarser than the DLR grid. Therefore the tip vortex of blade 1 can be traced much longer in the DLR grid than in the ONERA grid. This is again shown for x=6 where the 120^{o} old tip vortex of blade 1 (T1) is clearly represented in the DLR computation at y=-7, z=-2.

5. Conclusion

A comparison of the deforming grid (ONERA) and the chimera (DLR) Euler method for isolated rotors in high speed forward flight was carried out. It turned out that the way the region around the axis of rotation is discretized has considerable effects for $300^{o} < \psi < 360^{o}$ and for $0^{o} < \psi < 60^{o}$. The deforming mesh Euler method (ONERA) uses a so called artificial hub boundary at the blade root. This suppresses completely the downwash velocities at the downstream boundary of the artificial hub which leads to an overprediction of the z-forces on the blade for $0^{o} < \psi < 60^{o}$. The artificial hub boundary also suppresses the generation of root vortices. A root vortex increases the effective angle of attack for the following blade for $0^{o} < \psi < 60^{o}$. Suppressing the root vortex compensates to some extend the increase in effective angle of attack due to the artificial hub boundary. The chimera Euler method (DLR) does not use an artificial hub boundary. In order to ease the application of the chimera method each rotor blade is modelled without a shaft. Because of this the root section of the advancing blade in the first quadrant produces a root vortex which is considerably stronger than in the experiment.

Keeping this in mind the two methods which use completely different grid strategies are in excellent agreement which each other and in very good agreement with the experimental data.

As a general rule the grid should represent the blade root adequately in order to predict the correct effective angles of attack for $0^{o} < \psi < 60^{o}$. An artificial hub boundary in combination with a free stream condition should be avoided for forward flight applications. For a better resolution of the vortices much finer and very regular grids are needed.

6. Bibliography

[1] Boniface, J.-C.; Pahlke, K.
Calculations of multibladed rotors in forward flight using 3D Euler methods of DLR and ONERA
22nd ERF, Brighton (UK), September 17-19, 1996.

[2] Jameson, A.; Schmidt, W. and Turkel, E.
Numerical Solutions of the Euler Equations by Finite Volume Methods Using Runge-Kutta Time Stepping Schemes
AIAA Paper 81-1259.

[3] Pahlke, K.; Blazek, J. and Kirchner, A.
Time-Accurate Euler Computations for Rotor Flows
Royal Aeronautical Society, 1993 European Forum. Recent Developments and Applications in Aeronautical CFD. Bristol (UK), 1993.

[4] Kroll, N.
Berechnung von Strömungsfeldern um Propeller und Rotoren im Schwebeflug durch die Lösung der Euler-Gleichungen
DLR-FB 89-37.

[5] Benek, J.A.; Buning, P.G. and Steger, J.L.
A 3-D Chimera Grid Embedding Technique
AIAA 7th Computational Fluid Dynamics Conference, Cincinnati, Ohio (USA).

[6] Dougherty, F.C.
Development of a Chimera Grid Scheme with Applications to Unsteady Problems
Stanford University, Ph. D., 1985.

[7] Pahlke, K. and Raddatz, J.
Flexibility Enhancement of Euler Codes for Rotor Flows by Chimera Techniques
20th ERF, Amsterdam (The Netherlands), 1994.

[8] Findling, A.; Herrman, U.
Development of an efficient and robust solver for elliptic grid generation
Proceedings of the Third International Conference on Numerical Grid Generation in Computational Fluid Dynamics and Related Fields, Barcelona, Spain, 3.-7.6.1991.

[9] Lerat, A. and Sidès, J.
A New Finite-Volume Method for the Euler Equations With Applications to Transonic Flows
Proceedings of the Conference on Numerical Method in Aeronautical Fluid Dynamics, University of Reading, March 30-April 1, 1981. Edited by P.L. Roe, Academic Press, pp. 245-288, 1982.

[10] Sidès, J.
Computation of Unsteady Transonic Flows With an Implicit Numerical Method for Solving the Euler Equations
La Recherche Aérospatiale No. 2, 1985.

[11] Boniface, J.C., Mialon, B. and Sidès, J.
Numerical Simulation of Unsteady Euler Flows Around Multibladed Rotors in Forward Flight Using a Moving Grid Approach
AHS-51st Annual Forum and Display, Fort-Worth, TX(USA), 1995.

[12] Costes, M.; Houwink, R.; Kokkalis, A.; Pahlke, K.; Sapporiti, A.
Application of European CFD Methods for Helicopter Rotors in Forward Flight.
Eighteenth European Rotorcraft Forum, Paper 50, Avignon, 15.-18. September, 1992.

[13] Philippe, J.J. and Chattot J.J.
Experimental and Theoretical Studies on Helicopter Blade Tips at ONERA
6th ERF. Also TP ONERA 1980-96.

[14] Toulmay, F.
Modèle d'Etude de l'Aérodynamique du Rotor. Formulation et application
Aérospatiale Report H/D.E.R. 37176.

[15] Pahlke, K.
Extension of a 3D Time-Accurate Euler Code to the Calculation of Multibladed Rotors in Forward Flight without Wake Modelling
In ECARP II: Validation of CFD Codes and Assessment of Turbulence Models, paper II.11, Vieweg series 'Notes on Numerical Fluid Mechanics', edited by W. Haase, E. Chaput, E. Elsholz, M.A. Leschziner, U.R. Müller, 1996.

8. Figures

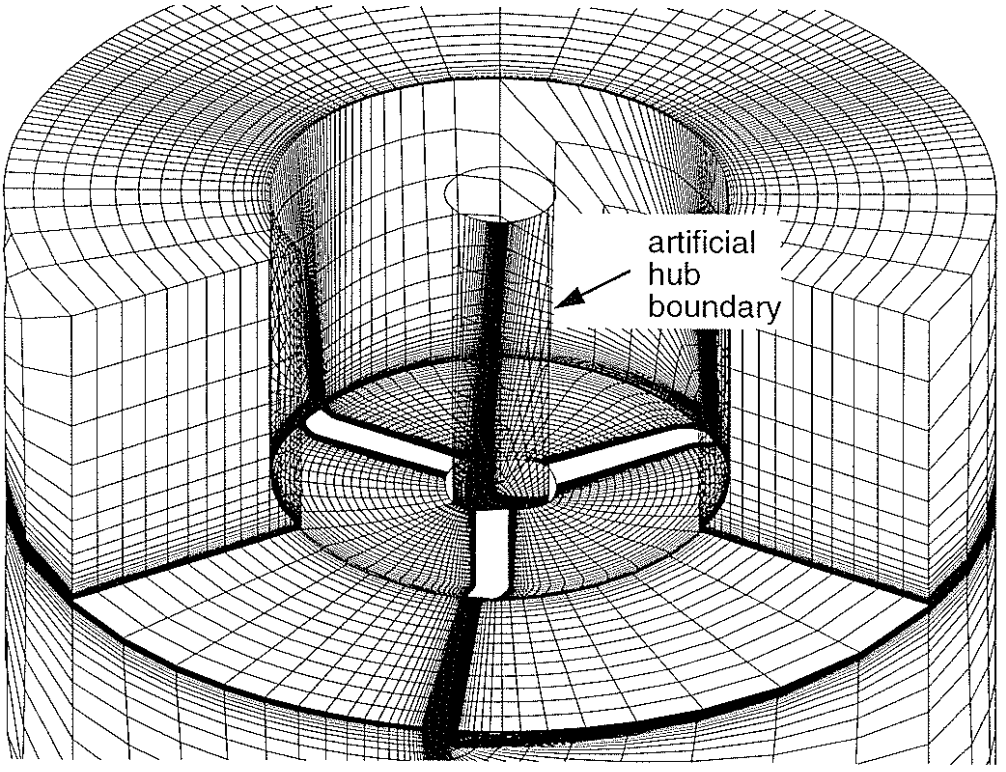

Figure 1: 3D view of the multiblock deforming grid

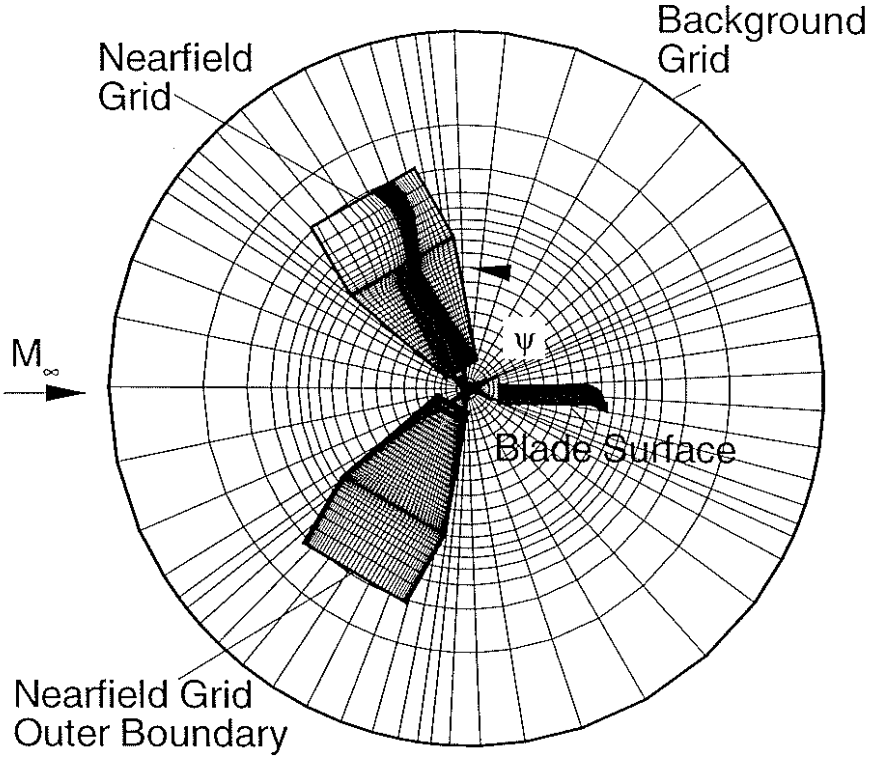

Figure 2: Top view of the chimera grid system

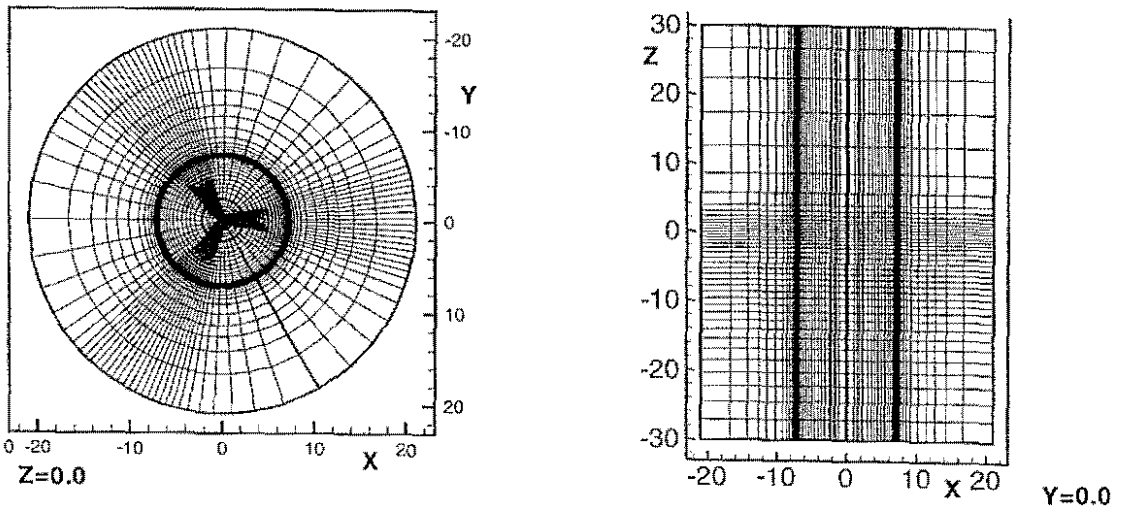

Figure 3: Top view (left) and y=0-Section (right) of the R_{FF}=3R-background grid

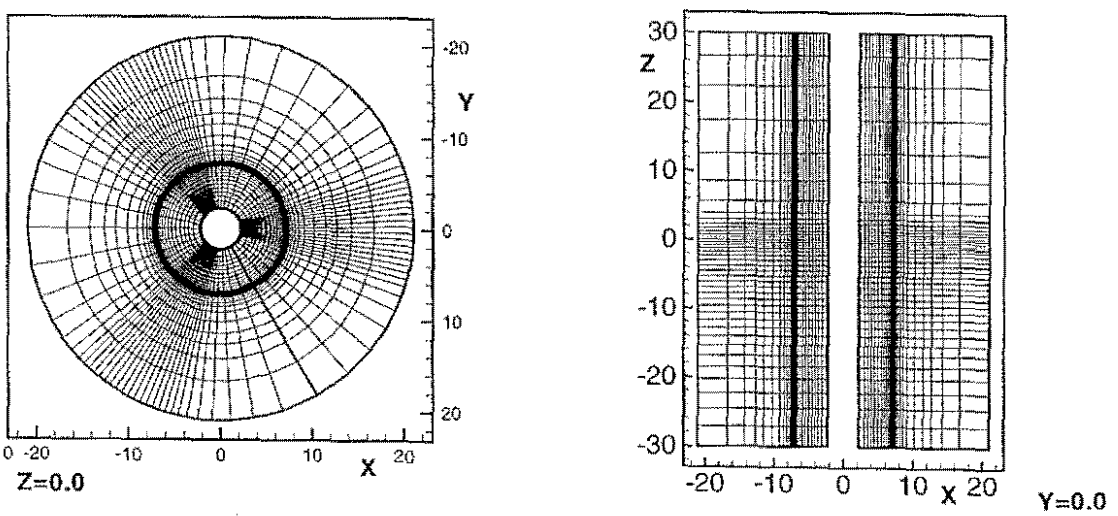

Figure 4: Top view (left) and y=0-Section (right) of the r_{hub}/R=0.3-background grid

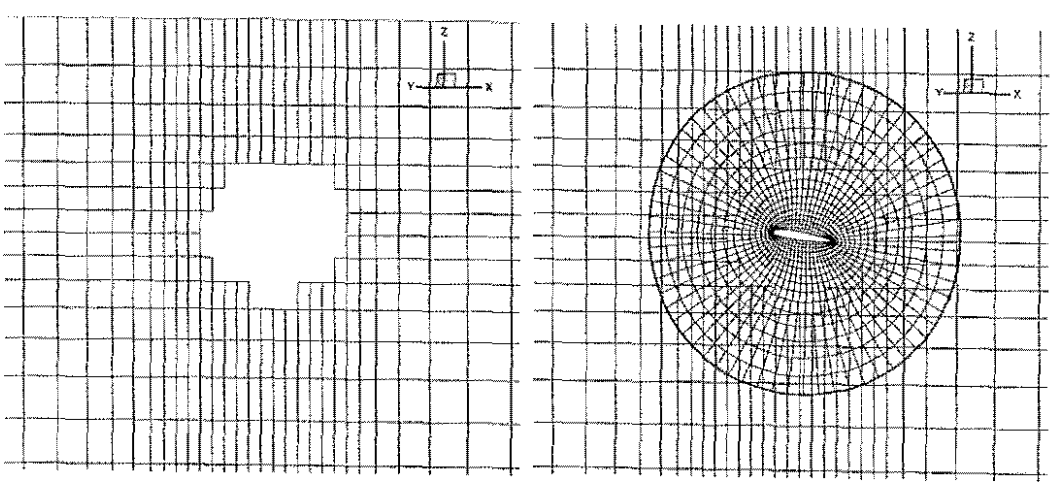

Figure 5: Grid of cell centers for the R_{FF}=3R-grid at 0.85R
Left: Background grid with hole cells blanked out
Right: Child grid embedded in background grid

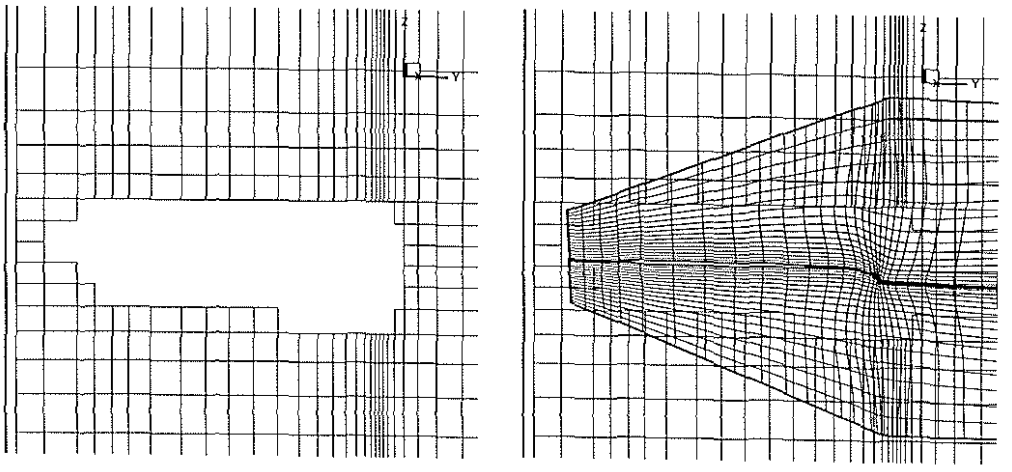

Figure 6: Longitudinal section through the grid of cell centers for the R_{FF}=3R-grid
Left: Background grid with hole cells blanked out
Right: Child grid embedded in background grid

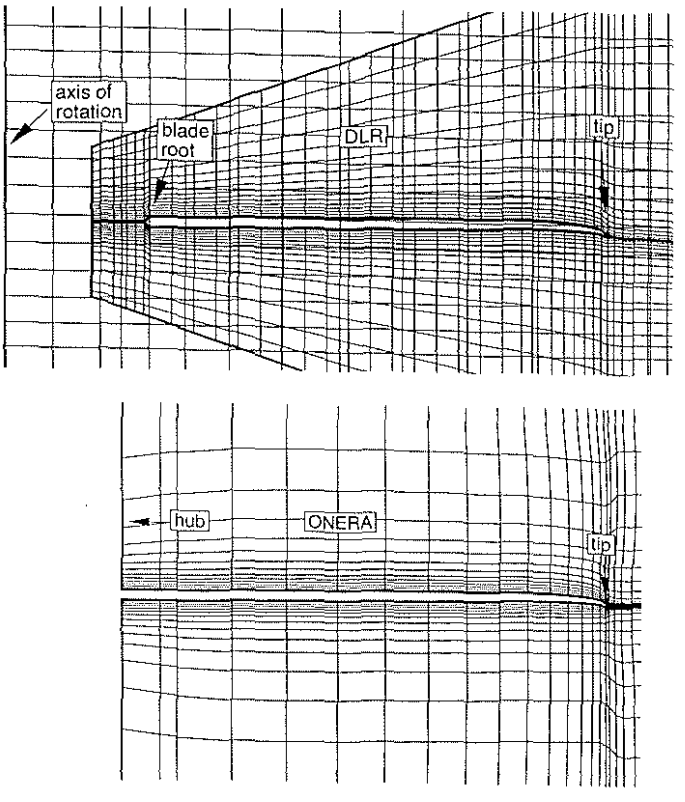

Figure 7: Longitudinal section through the overlapping grid (DLR) and the conventional grid (ONERA)

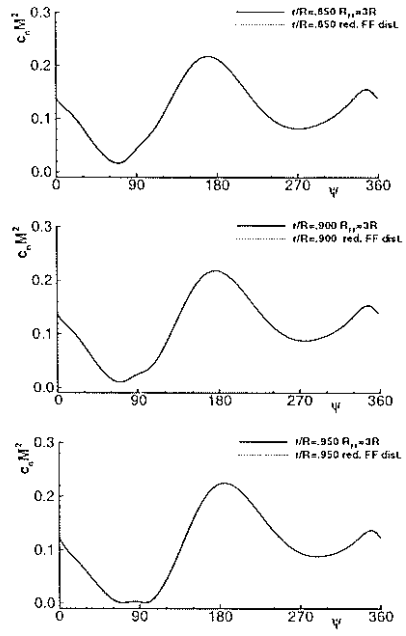

Figure 8: z-force-coefficients for two different farfield distances

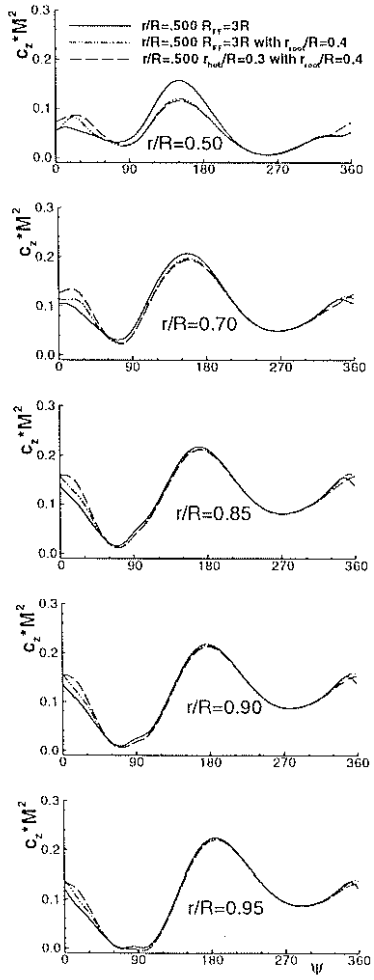

Figure 9: z-force-coefficients for computations with different blade root positions and a computation with a hub

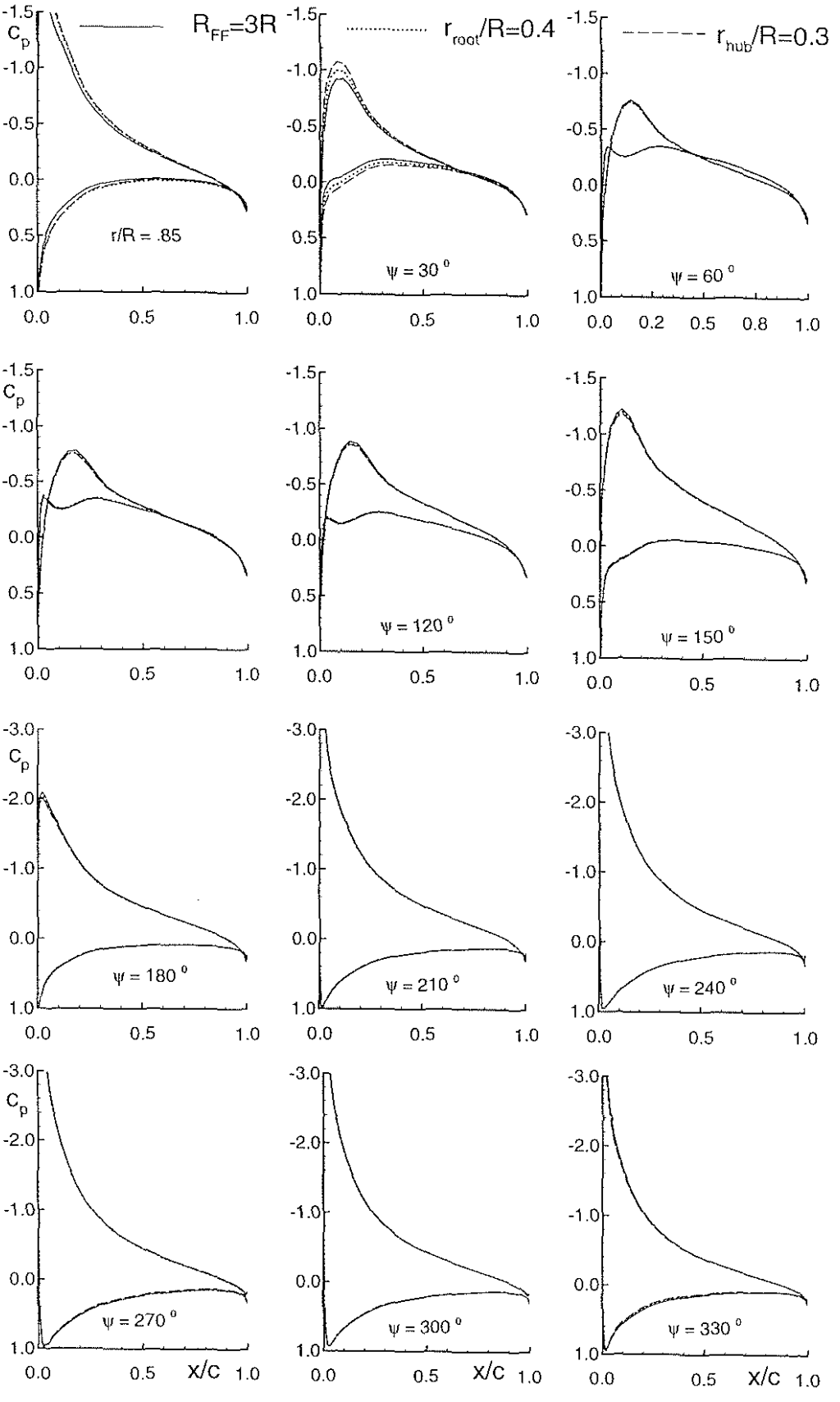

Figure 10: Pressure distributions for computations with different blade root positions and a computation with a hub at r/R=0.85

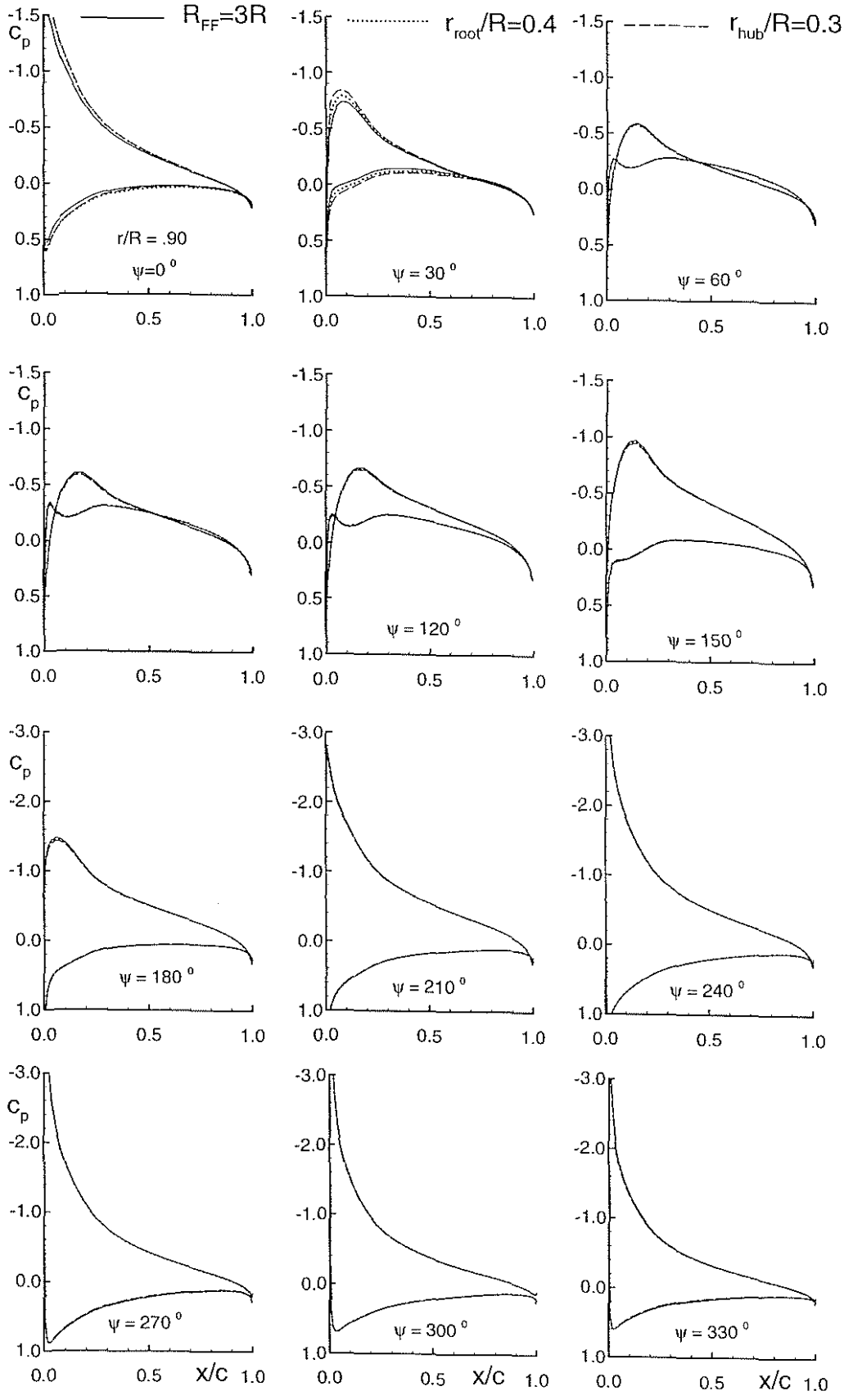

Figure 11: Pressure distributions for computations with different blade root positions and a computation with a hub at r/R=0.90

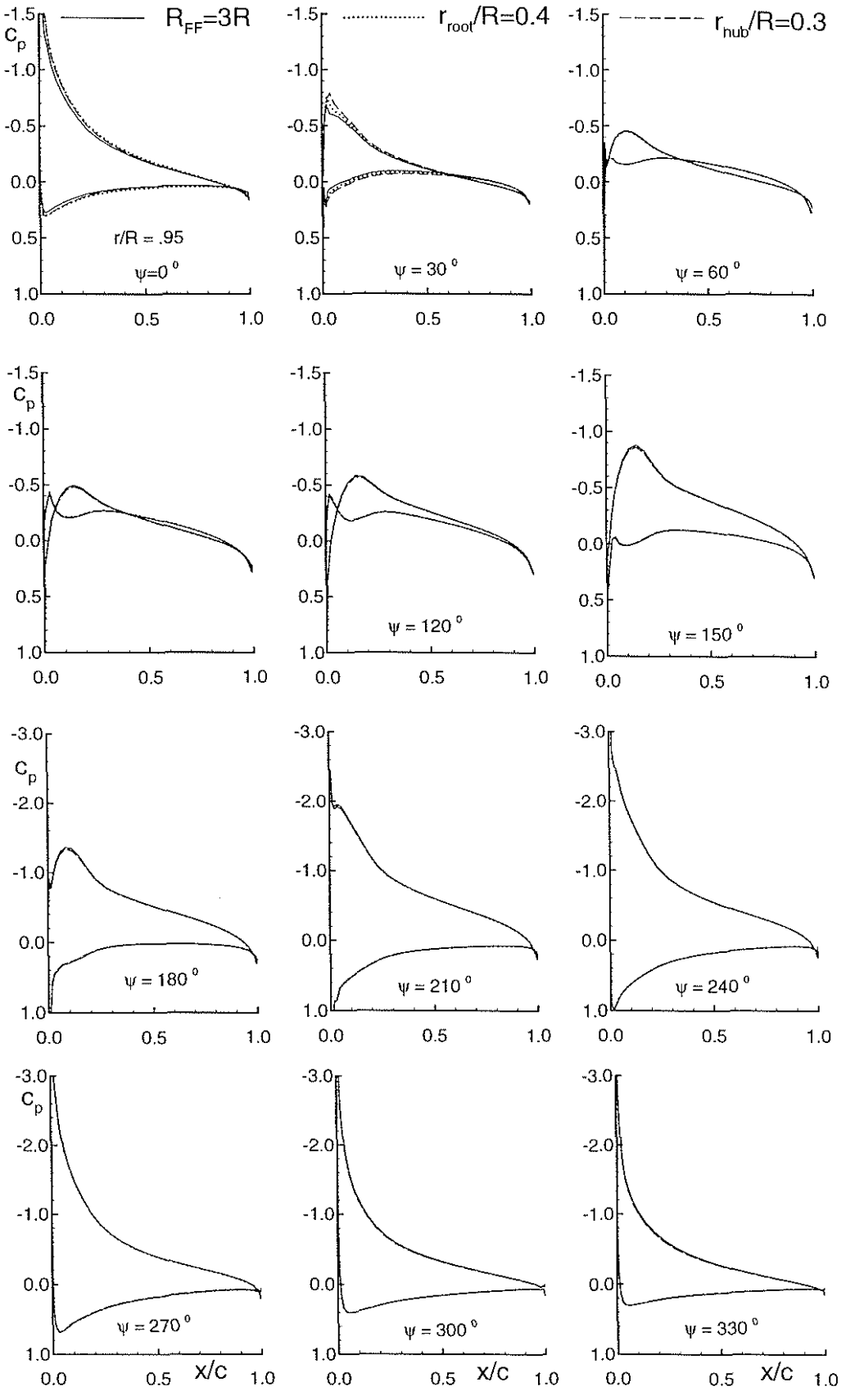

Figure 12: Pressure distributions for computations with different blade root positions and a computation with a hub at r/R=0.95

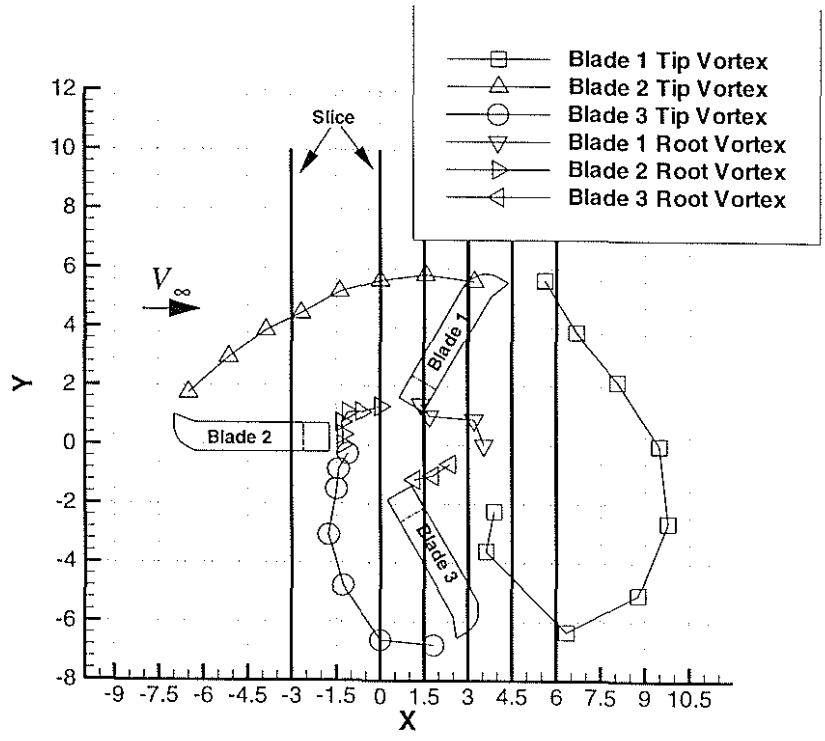

Figure 13: Vortices in a chimera computation with the R_{FF}=3R-grid ($\Psi_{Blade1}=60^0$)

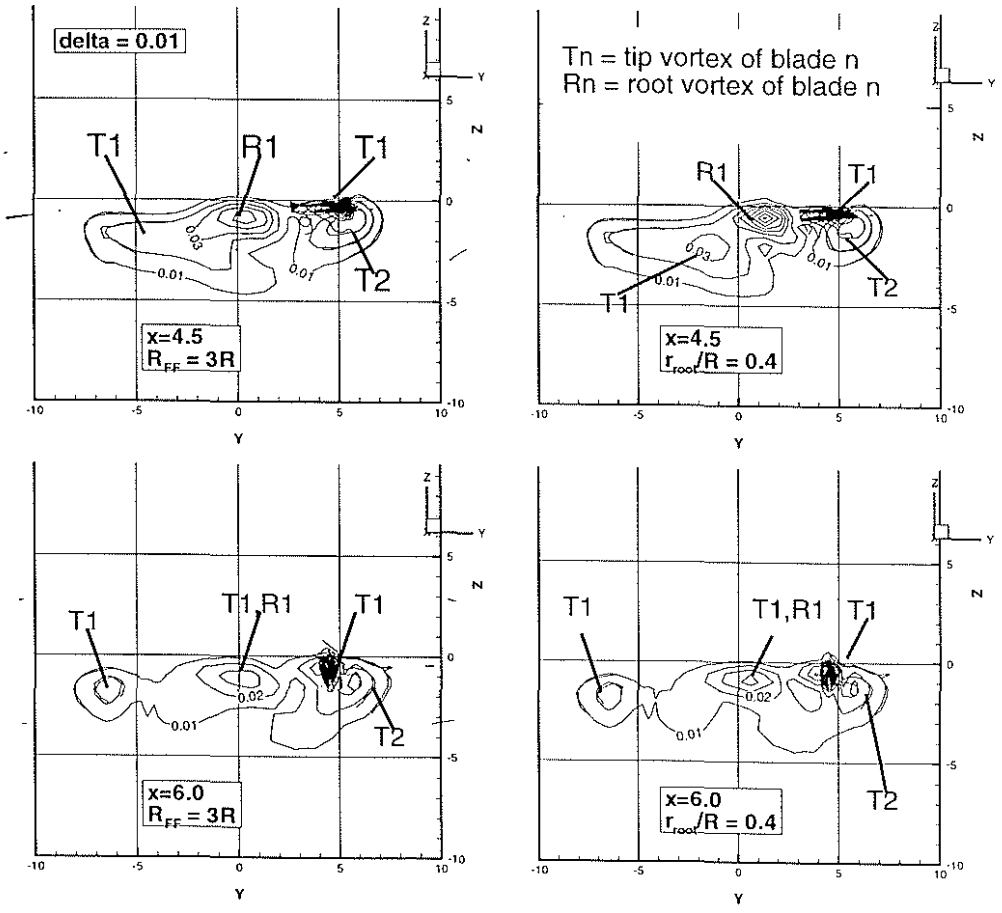

Figure 14: Vorticity distribution for x=4.5 and x=6 for two positions of the blade root

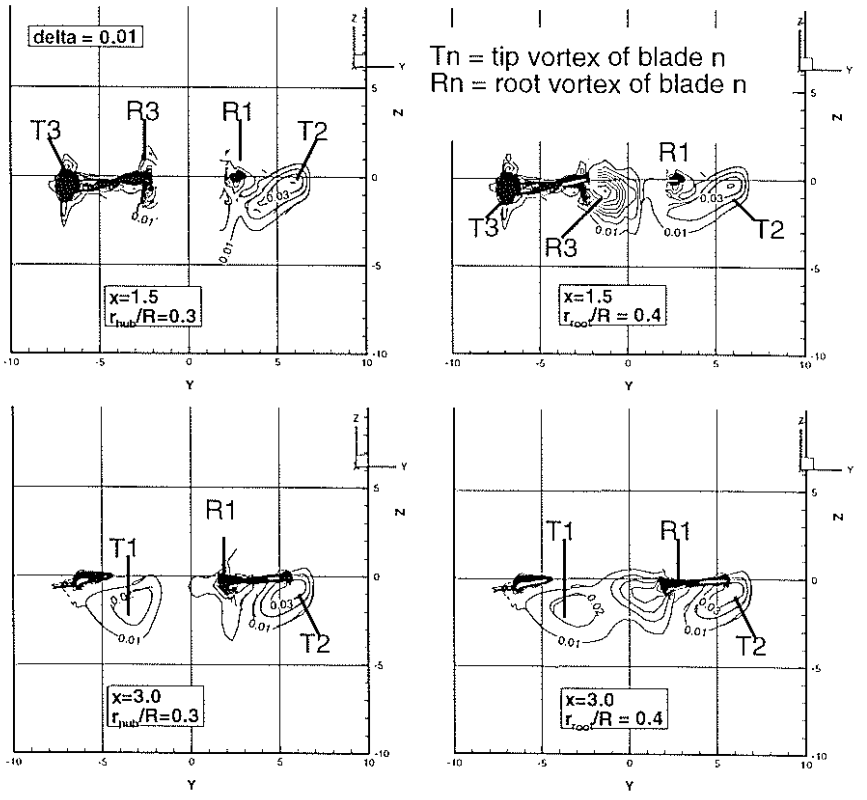

Figure 15: Vorticity distribution for x=1.5 and x=3 for a computation with hub (r_{hub}/R=0.3) and without hub (r_{root}/R=0.4)

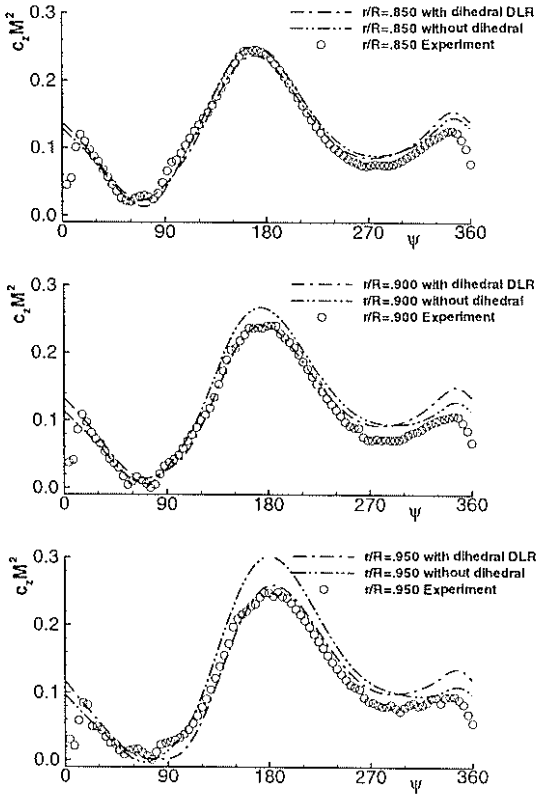

Figure 16: Effect of dihedral on z-force coefficient

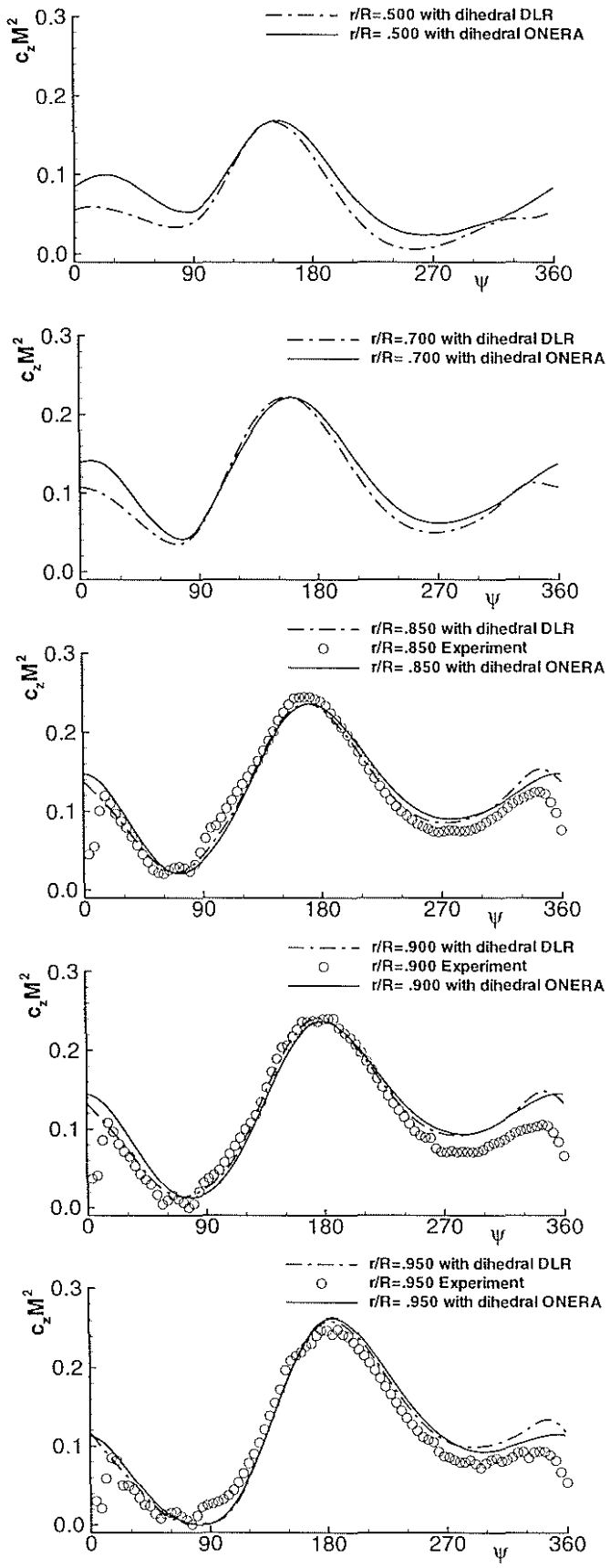

Figure 17: Comparison of ONERA and DLR z-force prediction with the experimental data

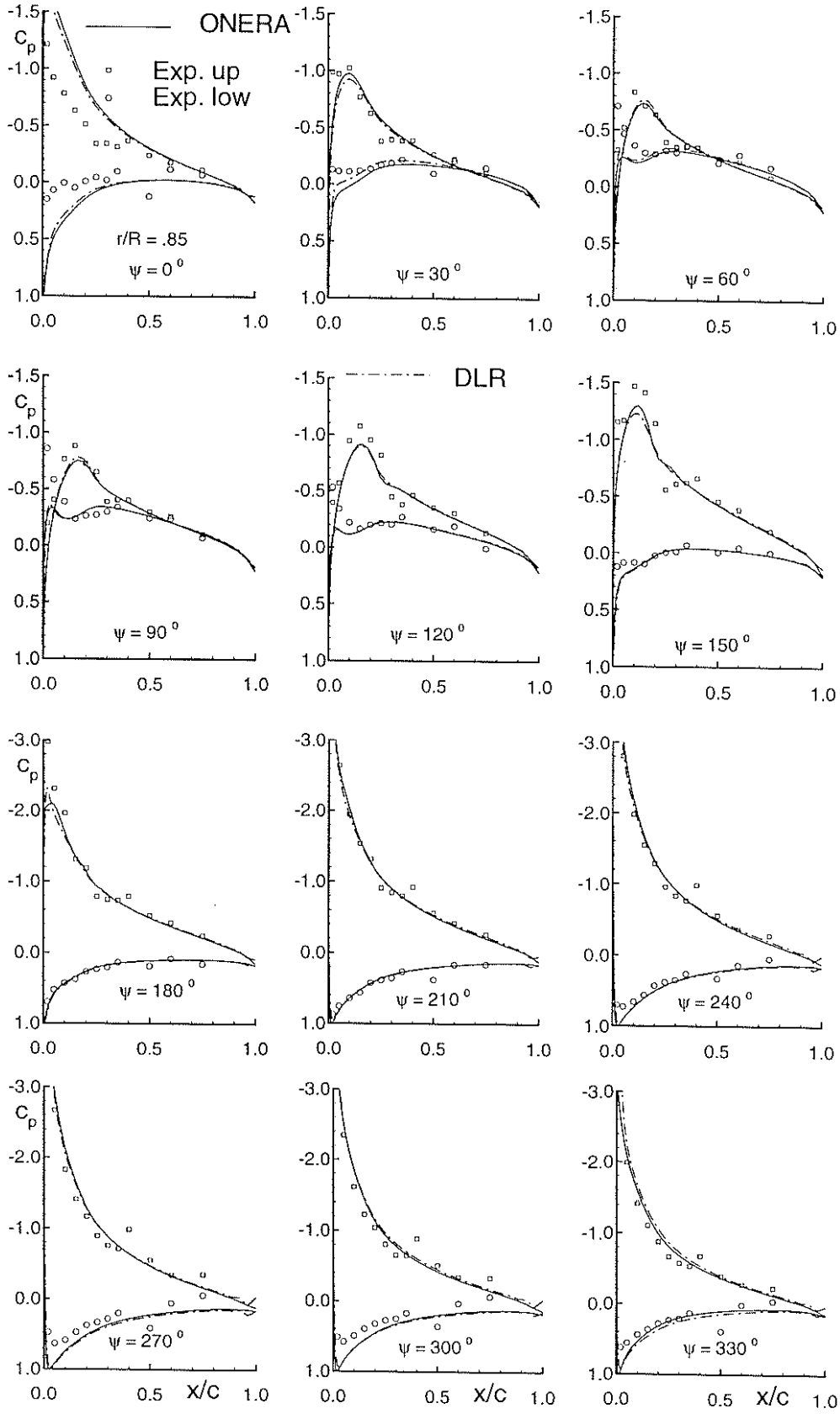

Figure 18: Comparison of ONERA and DLR pressure prediction with the experimental data at r/R=0.85

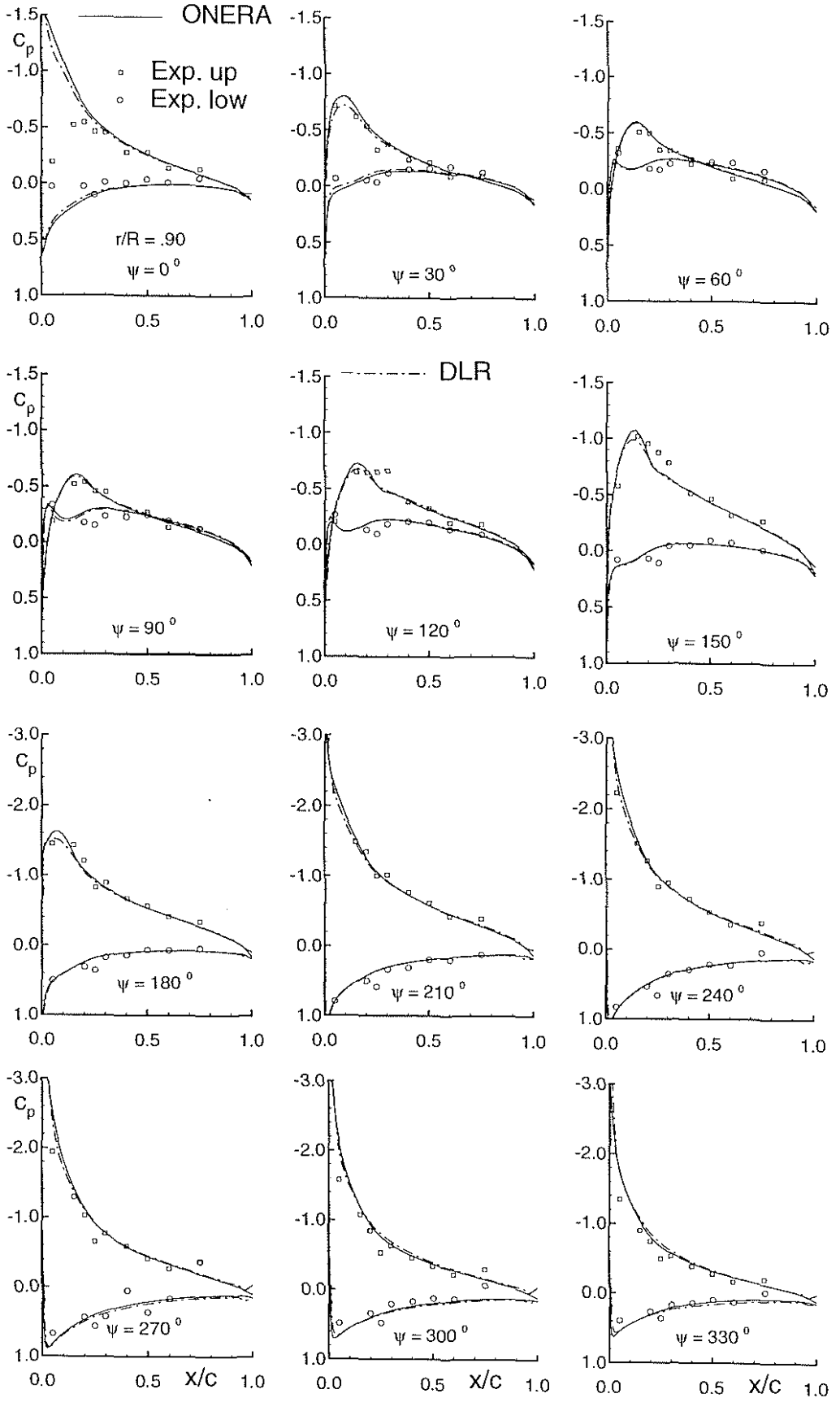

Figure 19: Comparison of ONERA and DLR pressure prediction with the experimental data at r/R=0.90

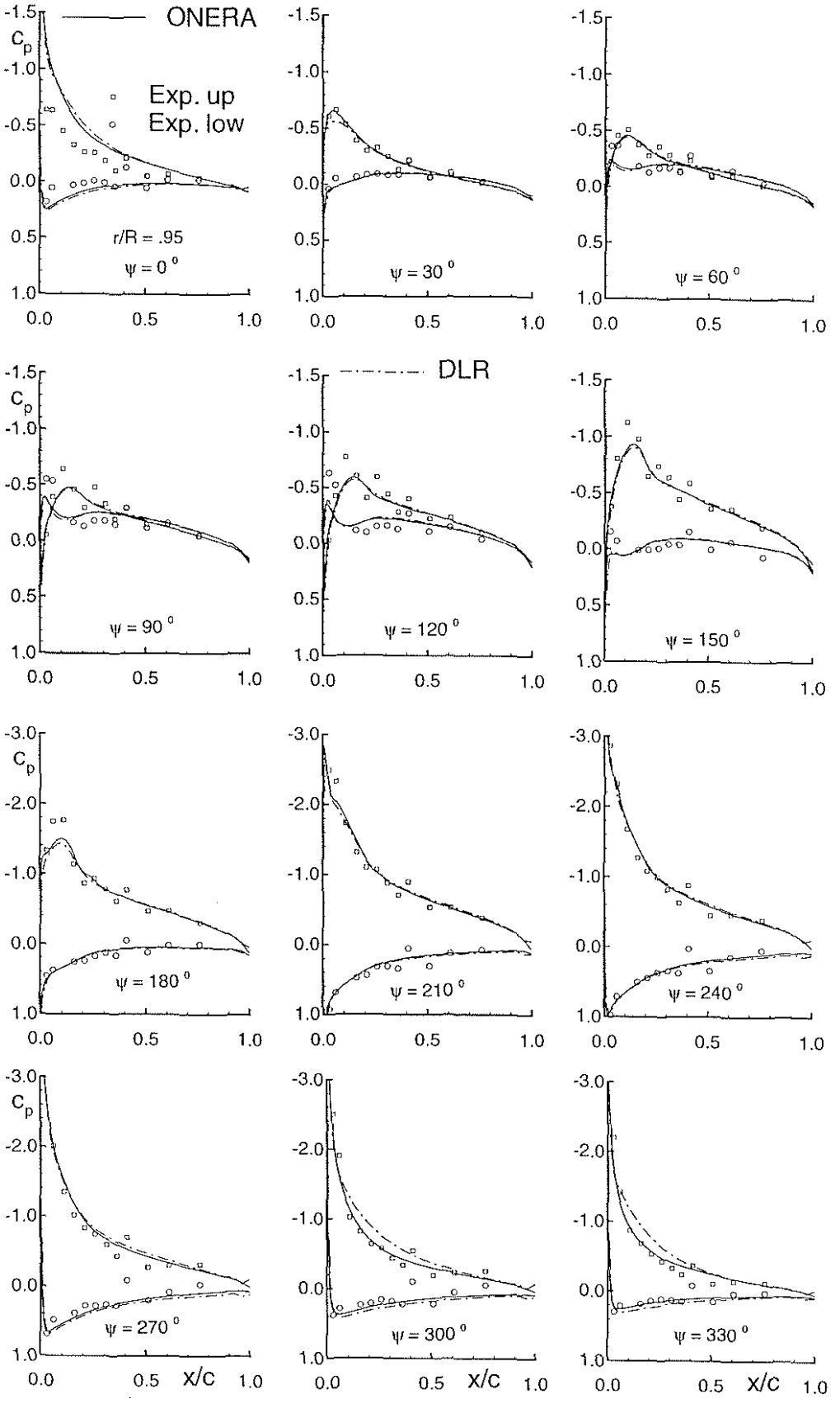

Figure 20: Comparison of ONERA and DLR pressure prediction with the experimental data at r/R=0.95

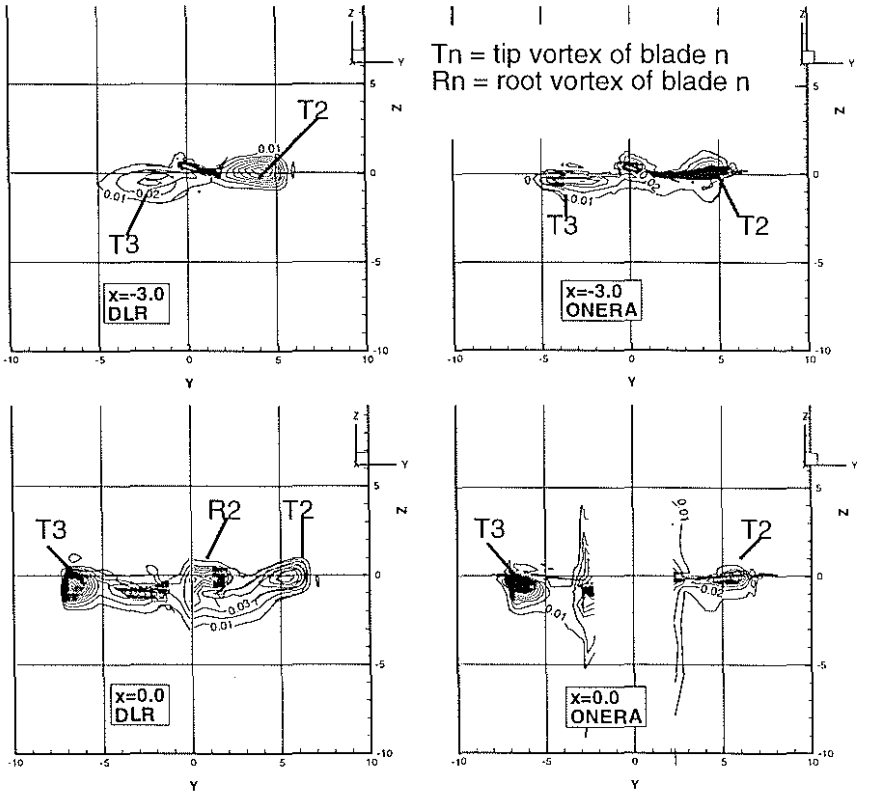

Figure 21: Comparison of vorticity distribution for ONERA and DLR computation (x=-3.0 and x=0.0)

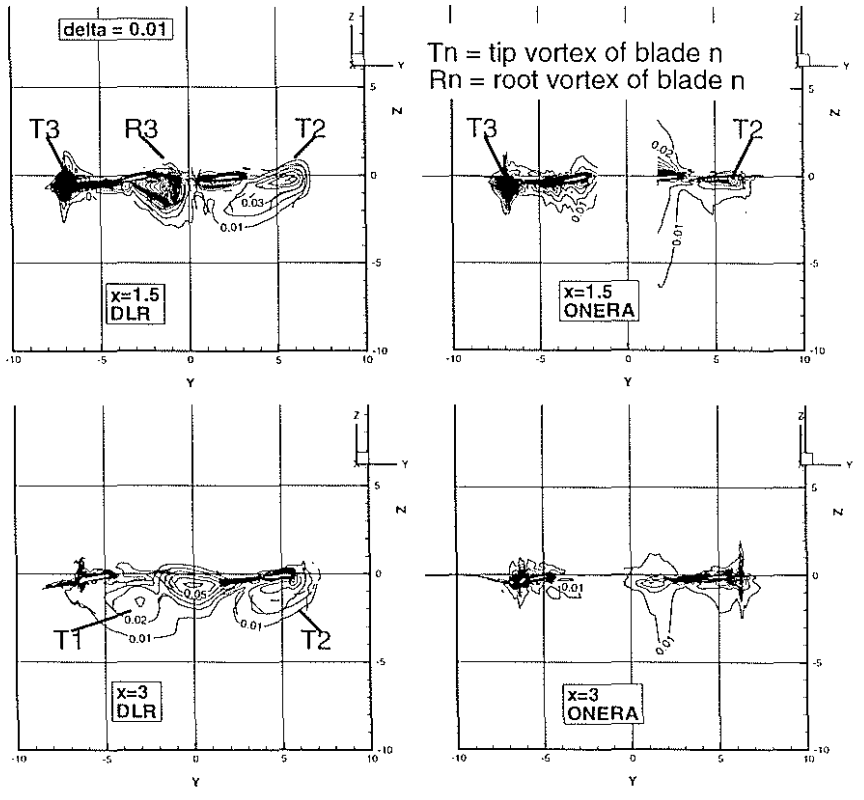

Figure 22: Comparison of vorticity distribution for ONERA and DLR computation (x=1.5 and x=3.0)

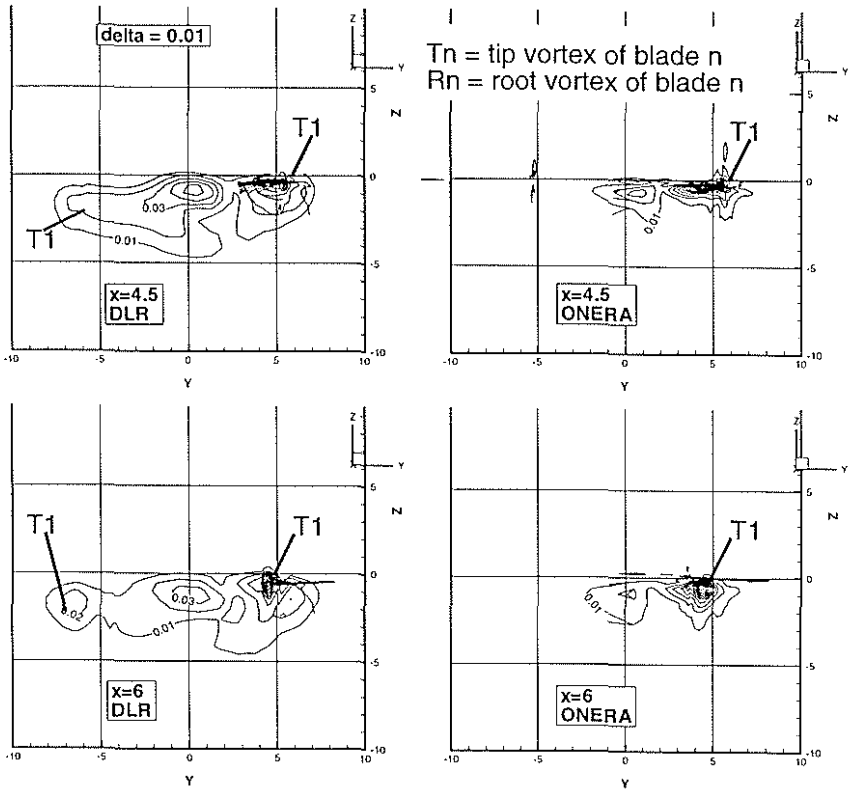

Figure 23: Comparison of vorticity distribution for ONERA and DLR computation (x=4.5 and x=6.0)